



# Diagnosis of Local Gravity Wave Properties during a Sudden Stratospheric Warming

Lena Schoon<sup>1</sup> and Christoph Zülicke<sup>1</sup>

<sup>1</sup>Leibniz-Institute of Atmospheric Physics, Schlossstrasse 6, 18225 Kühlungsborn, Germany

Correspondence to: Lena Schoon (schoon@iap-kborn.de)

**Abstract.** Commonly, wave quantities are maintained in zonal mean averages. Hence, local wave phenomena remain unclear. Here, we introduce a diagnostic tool for studies of wave packets locally. The “Unified Wave Diagnosis” (UWaDi) uses the Hilbert Transform to obtain a complex signal from a real-valued function and estimates the amplitude and wave number locally. Operational data from the European Centre for Medium-Range Weather Forecasts is used to perform the analysis.

5 Restrictions on gravity wave propagation due to model sponge layers are identified well above the 10 hPa altitude. From a minor stratospheric warming in January 2016 three cases for vertical gravity wave propagation in different background wind conditions are selected. It is shown that zonal mean wind quantities cannot reveal local “valves” allowing gravity waves to propagate into the mid-stratosphere. The unexpected finding of high gravity wave activity at the minor warming of 30 January 2016 is related to strong planetary wave activity and a strong local “pump”. Accordingly, the advantages of a local wave packet

10 analysis are demonstrated for profiles up to the model sponge layer.

## 1 Introduction

Gravity waves (GWs) have been subject of intense research during the past decades. The scales of GWs reaching from planetary scales ( $\approx 1000$  km) to turbulent microscales ( $\approx 10$ m) create a broad field of interest in their role in coupling processes of atmospheric dynamics (Fritts and Alexander, 2003). A phenomenon associated with huge changes in GW appearance is a sudden stratospheric warming (SSW). During a SSW event the middle atmosphere is characterised by three different background wind conditions during a short period of time. Starting with normal winter conditions, followed up by summer-like conditions and a slowly transfer back to winter conditions. Respectively, GW variability is associated with changing background wind conditions. Defined by the World Meteorological Organization SSWs are characterised by a reversal of the  $60^\circ$  N to  $90^\circ$  N-temperature gradient. Major warmings are, additionally, associated with a wind reversal at 10 hPa and  $60^\circ$  N, minor SSWs

20 (mSSWs) with a wind deceleration at 10 hPa and  $60^\circ$  N, where the prevailing westerlies are not turned into easterlies. Planetary waves (PWs) play a crucial role in the driving of a SSW event (Andrews et al., 1987). Nevertheless, on the one hand GWs are affected by different background wind conditions that are characteristic during SSWs, on the other hand they are suspected to take, even though a minor, part in the modification of the polar vortex prior to SSWs (Albers and Birner, 2014). Variations in background wind conditions establish zones with wave guides where GWs can propagate easily to higher altitude, as well as

25 forbidden zones of GW propagation (Dunkerton and Butchart, 1984). Models and simulations give the opportunity to analyse



the behaviour of GWs and PWs during SSWs up to the mesosphere and lower thermosphere (Liu and Roble, 2002; Limpasuvan et al., 2011, 2012; Hitchcock and Shepherd, 2013; Miller et al., 2013; Albers and Birner, 2014). These studies dealing with GW momentum fluxes are verified by radar measurements (De Wit et al., 2015) as well as satellite observations (Limpasuvan et al., 2011; Yamashita et al., 2013; Thurairajah et al., 2014; Jia et al., 2015; Ern et al., 2016). Ern et al. (2016) point out that the zonal average view of GW parameters that are mainly extracted of models is misleading and local GW activity can vary strongly, especially during SSWs. Next to critical levels, where GWs slow down and eventually dissipate, local regimes of "valves" or "bottlenecks" occur, where the transmission of GWs into the middle stratosphere depends very sensitively on the local wind (Zülicke and Peters, 2008; Kruse et al., 2016). Here we study a minor warming in January 2016 as a test case for local specific propagation conditions for GWs.

Assimilated data products from the European Centre for Medium-Range Weather Forecasts (ECMWF) are suitable to analyse local phenomena and their coupling, as they resolve essential parts of GW dynamics in the stratosphere, sufficiently. The T799 resolution already gives proof of correct GW appearance in the stratosphere. Validation with satellite measurements point out that ECMWF GWs from the tropics are not realistic (Preusse et al., 2014), but mid- and high-latitude GWs are captured well by ECMWF analysis (Yamashita et al., 2010). The recently introduced and improved T1279 resolution yields to a bigger portion of resolved GWs in ECMWF data. Even though the tropical portion of parameterised convective GWs is still too small, mid-latitude GWs are captured well being driven by orographic and jet-stream associated sources (Shutts and Vosper, 2011). A comparison with balloon-borne measurements on the southern hemisphere shows an underestimation of momentum fluxes by the factor of 5 of ECMWF GWs in mid-latitudes but the overall appearance and propagation of GWs are realistic (Jewtoukoff et al., 2015). Hence, ECMWF resolved GWs meet our requirements to identify local valves. In particular, we want to investigate local quantities of resolved GWs in the ECMWF analysis for different background wind conditions. In order to perform such an analysis, the GW amplitudes and wave numbers need to be locally diagnosed in three dimensions.

Another issue is the search for varying GW sources because there is some likeliness that strong PWs govern jet streaks. From their exit regions GWs may be radiated by spontaneous imbalance which may "pump" them into the middle atmosphere (Uccellini and Koch, 1987; O'sullivan and Dunkerton, 1995; Plougonven et al., 2003). Several methods to extract wave properties can be found in literature. Most of these methods are linked to a limited range of wave frequencies and/or special observation techniques. Hence, most of these methods provide wave properties by spatial averaging and therefore accept a loss of information. Starting with the analysis of PWs, two-dimensional zonal-mean effects can be described by the Eliassen-Palm flux (Andrews et al., 1987). Extended studies on three-dimensional wave propagation yield to the wave activity flux (WAF) (Plumb, 1985, 1986) with an analogue for GWs, the gravity wave flux (Bretherton, 1966). The unification of these fluxes lead to a three-dimensional WAF describing wave propagation both for inertia GWs and PWs (Kinoshita and Sato, 2013a). Further studies provide corrections for more accurate magnitudes and directions of wave propagation (Kinoshita and Sato, 2013b) as well as a separate formulation for equatorial waves (Kinoshita and Sato, 2014). While these approaches are designed to estimate the pseudo-momentum flux, a more kinetically oriented approach asks for wave amplitudes and wave numbers. A common approach to obtain vertical wave numbers and GW frequency of high-passed filtered data are Stokes parameters (Vincent and Fritts, 1987). This method works for single vertical measurements and provides the wave properties in several vertical height sections.



Another method that is capable to derive wave numbers in all three dimensions uses auto-covariance functions defined over spatial-averaged boxes (Zülicke and Peters, 2006). Therein, it is utilised that the use of the horizontal divergence simplifies the harmonic analysis by neglecting geostrophic flow by definition and redundantises filtering processes. Local wave properties are obtained by an one-dimensional signal-processing technique named the Hilbert Transform. Zimin et al. (2003) introduce the method by providing the amplitude of a wave packet for an arbitrary set of waves. Rewriting the formulation to work on streamlines makes it more adaptable to various quasi one-dimensional propagations of wave packets (Zimin et al., 2006). An adaption to Rossby wave trains shows good results and recommends this approach (Glatt and Wirth, 2014). Furthermore, it is generalised for different directions addressing multi-dimensional problems by Sato et al. (2013).

With this paper we introduce a new method to obtain phase-independent wave properties locally. The vertical propagation of GWs during different background wind conditions induced by a mSSW serves as an example to detect local valves in vertical GW transmission. ECMWF reanalysis data are chosen to meet our requirements. The paper is organised as follows. After providing an overview of the newly developed method to obtain wave properties locally in Sect. 2, two synthetic examples of wave packets are given to validate and demonstrate the advantages of the new algorithm. This section is followed by a description of the used ECMWF data and the wave quantities needed for the analysis of GW properties during a SSW. In Sect. 3 three time phases around a mSSWs in January 2016 are investigated for valves of vertical wave transmissions: the prewarming, midwarming and postwarming phase. A summary, discussion and outlook are found in Sect. 4.

## 2 Method and data

Hereafter, we develop and validate an algorithm to extract wave parameters from an equidistant three-dimensional data. It reads, processes and plots autonomously, accepting user-defined flags in an attached namelist. For local diagnosis of waves, e.g. inertia gravity waves, phase-independent estimates are essential. Therefore, complex quantities are constructed for an amplitude-phase presentation by a Hilbert Transform (Von Storch and Zwiers, 2001; Zimin et al., 2003; Sato et al., 2013). Additionally, wave numbers are estimated. We call this procedure "Unified Wave Diagnosis" (UWaDi). The method is sketched briefly.

### 2.1 Unified Wave Diagnosis

Complex values of a function  $f[x]$  are found with the Hilbert Transform in x-direction:

$$\hat{f}[x] = f[x] + iH(f[x]). \quad (1)$$

The Hilbert Transform provides a new complex series  $\hat{f}[x]$  compounded of the sum of the original function  $f[x]$  as the real part and the Hilbert-transformed series  $H(f[x])$  as the imaginary part. Literally, the Hilbert Transform shifts  $f[x]$  a quarter to the right  $(-\frac{\pi}{2})$  turning a cosine into a sine and a sine into a minus cosine.



The Hilbert Transform itself is composed of three steps (Zimin et al., 2003). First, a discrete Fourier Transform (DFT) is conducted

$$f[k] = \text{DFT}(f[x]), \quad (2)$$

followed by an user-defined bandpass filtering process ( $0 < k_{min} < k_{max}$ )

$$5 \quad f_{filtered}[k] = F(k_{min}, k_{max})f[k], \quad (3)$$

and an inverse DFT

$$\hat{f}[x] = 2 * \text{DFT}^{-1}(f_{filtered}[k]). \quad (4)$$

Using this complex series, we estimate the amplitude and wave number of a wave packet.

The amplitude is maintained by (Schönwiese, 2013)

$$10 \quad a[x] = |\hat{f}[x]| = \sqrt{f[x]^2 + H(f[x])^2} \quad (5)$$

and gives an estimate of the local envelope of an oscillating function.

The phase  $\Phi$

$$\Phi[x] = \text{atan}\left(\frac{H(f[x])}{f[x]}\right) \quad (6)$$

is used to derive the absolute wave number

$$15 \quad k_x[x] = \frac{d\Phi[x]}{dx}. \quad (7)$$

By highlighting the use of UWaDi for three-dimensional data the wave number-weighted three-dimensional quantities are the main gain

$$a_{final}[x, y, z] = \sqrt{\frac{\sum_d q_d k_d^2 a_d^2}{\sum_d q_d k_d^2}} \quad (8)$$

and

$$20 \quad k_{final}[x, y, z] = \sqrt{\sum_d q_d * k_d^2} \quad (9)$$

with  $d = [x, y, z]$ . By using this method, wave properties for every dimension  $d$  are obtained separately and get combined in the last step of the algorithm to a three-dimensional field of local wave properties.  $q$  denotes the quality flag. Included are different quality checks. First, the amplitude and wave number are checked for at least a half undamped wave considering the packet length  $l$  ( $k \times l > \pi$ ). Second, noise suppression is considered by taking into account the standard deviation of the data and creating a threshold under which results are rejected (Glatt and Wirth, 2014). Third, high frequency fluctuations in amplitude and wave number are smoothed by a running mean over a number of grid points, respecting the minimum wave number  $k_{min}$  of the bandpass filter.

This method does not cover the temporal propagation of a wave packet and therefore the wave number misses sign ( $k = \pm k[x]$ ).

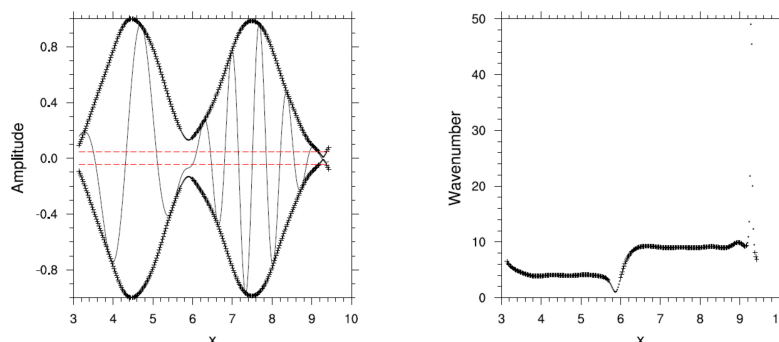


**Figure 1.** One-dimensional test function (bold line, left figure) adapted from Zimin et al. (2003). UWaDi-calculated amplitude enveloping the test function (left) with crosses marking valid values according to the quality check. Additionally, the red lines specify thresholds belonging to the quality check which suppresses noisy signals. The calculated wave number (right) uses the same markers.

## 2.2 Analytical test case

Synthetical one- and two-dimensional test cases are considered to proof the reliability of UWaDi.

### One-dimensional wave packet

An one-dimensional example is adapted from Zimin et al. (2003). Two consecutive wave packets with the wave numbers 4 and 9 are given by

$$f[x] = \exp\left[-(x - 4.5)^2\right] \cos(4x) + \exp\left[-(x - 7.5)^2\right] \cos(9x). \quad (10)$$

UWaDi is performed for bandpass limits of wave numbers of 1 and 10. The amplitude peaks with 1.0 and envelopes the consecutive wave packets well (Fig. 1). Crosses mark the calculations passing the quality checks. The red lines show the threshold under which calculated values are treated as noise. This threshold can be chosen by the user to suit the individual problem. A small gap in valid amplitude values occurs at the transition between both wave packets, helping the user to distinguish between several wave packets in the analysis. The wave number shows fluctuations in areas where the amplitude becomes small. These are artefacts from the DFT and not considered as they do not pass the quality checks. We admit that the calculation of wave number is less unique but the wave numbers 4 and 9 are distinguishable. Hence, the method performs well in regions with sufficiently large amplitudes of the carrier waves.

### Two-dimensional wave packet

A two-dimensional wave packet is given by

$$f[x, z] = a \exp\left(-\left(\frac{z'^2}{l_z'^2} + \frac{x'^2}{l_x'^2}\right)\right) \cos(k_z z' + k_x x') \quad (11)$$

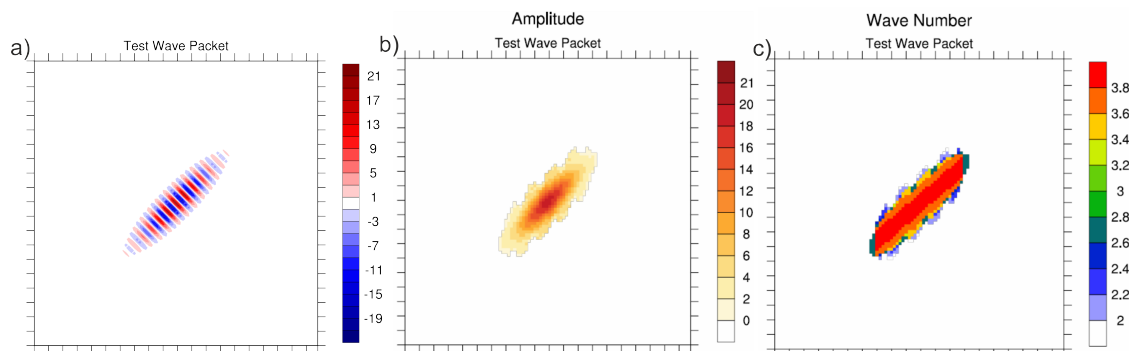


**Figure 2.** Two-dimensional test wave packet. a) Test wave packet according to Equation 11. b) Amplitude calculated by UWaDi and c) wave number in two-dimensional combination by UWaDi.

with an adapted coordinate system that might be rotated by  $\alpha$

$$x' = x \cos(\alpha) + z \sin(\alpha), \quad z' = -x \sin(\alpha) + z \cos(\alpha). \quad (12)$$

For this study following parameters are chosen:

$$l'_x = 4, \quad l'_z = 1, \quad a = 21, \quad k_x = 4, \quad k_z = 0, \quad \alpha = \frac{\pi}{4}.$$

5 Figure 2a shows the wave packet build by Equation 11.

The amplitude peaks with 21 (Fig. 2b) and the wave number with 3.8 (Fig. 2c). The edges of the wave packets in amplitude and wave number are not sharply contoured and show decreases of values to the edge, which is due to the small amplitude of the wave packet to its boundaries, as previously reported. Hence, the amplitude is captured well and the wave number estimation differs just slightly (about 5 %) from the input value.

10

The one- and two-dimensional wave packets had been further analysed in different noisy backgrounds and for several tilts. Effects on amplitude and wave number are negligible. Furthermore, one can envision that UWaDi may underestimate wave packets at the boundaries of the input field due to finite data strings in the DFT. Indeed, as long as the wave packet is one wavelength away from the field boundaries, UWaDi gives reliable results.

## 15 2.3 Data

ECMWF data from the Integrated Forecasting System (IFS) is chosen for this analysis. The IFS builds the base for the forecasts of ECMWF. The chosen data set has the spectral resolution T1279 ( $0.125^\circ \times 0.125^\circ$  longitude-latitude grid, ca. 16 km grid spacing) and L137 (number of model levels, reaching up to ca. 80 km altitude). The temporal resolution is 6 hours. Recent studies showed that ECMWF IFS data captures seasonal and geographical GW variability up to the lower stratosphere in mid- and high-latitudes (Wu and Eckermann, 2008; Yamashita et al., 2010; Shutts and Vosper, 2011; Preusse et al., 2014; Jewtoukoff et al., 2015).



Vertical propagating GWs are damped in ECMWF IFS products from 10 hPa ( $\approx 30$  km) upwards (ECMWF, 2016). At 10 hPa the stratospheric sponge starts and a damping of wave propagation is expected. The mesospheric sponge follows at 1 hPa acting on the divergence and therefore directly on the GW properties.

For this analysis the primary T1279 resolution is restricted to an  $1^\circ \times 1^\circ$  longitude-latitude grid to resolve mesoscale GWs (5  $\approx 200$  to 2000 km). The sampling theorem indicating that signals above the length of two times the grid space are captured, therefore allows for a detection of 222 km horizontal wavelength. The vertical level spacing in the stratosphere is about 1 km, which allows for a presentation of 2 km vertical wavelength in this analysis.

UWaDi requires an equidistant grid in all three dimensions. To overcome this issue, the Weather and Research Forecasting (WRF) Preprocessing System (WPS) is used. It is a tool to convert a model grid to an equidistant grid (cartesian coordinate system) (Skamarock et al., 2008). In order to select GW-relevant scales, we band-passed for a longitudinal set of wavelength between  $\lambda_x = [300\text{km} \dots 1500\text{km}]$ , the meridional range of wavelength is chosen to be  $\lambda_y = [700\text{km} \dots 3000\text{km}]$  and for the vertical GWs we set the limits to  $\lambda_z = [1\text{km} \dots 15\text{km}]$ .

## 2.4 Wave quantities

We choose the horizontal velocity divergence ( $\delta = \frac{\partial u}{\partial x} + \frac{\partial v}{\partial y}$ ) as the target quantity. By this, we operate on ageostrophic fields which contain essential parts of GW fluctuations without applying any numerical filtering procedure to separate wave and mean flow (Zülicke and Peters, 2006). From the diagnosis of this field, the amplitude ( $a$ ) and the wave numbers ( $k_x, k_y, k_z$ ) are obtained.

The kinematic wave energy (that is energy per mass, in units  $[\text{m}^2\text{s}^{-2}]$ ) is derived from polarisation equations assuming hydrostatics (Zülicke and Peters, 2006)

$$20 \quad e = \frac{s_\delta^2}{k_h^2} = \frac{a^2}{2} \frac{1}{k_x^2 + k_y^2}, \quad (13)$$

presuming the definition of signal processing techniques that the variance is expressible of terms of the amplitude:  $s^2 = \frac{a^2}{2}$ .

The wave action is a conserved quantity describing waves in the presence of background wind but not interacting with the mean flow (Bretherton, 1966). The wave action is defined by putting the kinematic wave energy  $e$  in relation to the intrinsic frequency  $\Omega$ :

$$25 \quad A = \rho \frac{e}{\Omega}, \quad (14)$$

$\rho$  being the density. The intrinsic frequency  $\Omega$  is calculated by the dispersion relation:  $\Omega^2 = f^2 + \frac{N^2(k_x^2 + k_y^2)}{k_z^2}$ .

Say  $A = \rho \frac{e}{\Omega} = \text{constant}$ , one can see the following

- density effect:  $e \propto \frac{1}{\rho} \propto \exp\left(\frac{z}{H}\right)$ . The above derived energy undergoes an exponential increase according to the density with the scale height  $H$  in vertical direction  $z$ .
- 30 – wind effect:  $e \propto \Omega$ . From the apparent phase speed  $c = \frac{\Omega}{k} + u$  one gets the dependence of the intrinsic frequency:  $\Omega = k(c - u)$ . Assuming constant phase speed  $c$  and a constant wave number  $k$  for a wave packet, meaning that a wave is

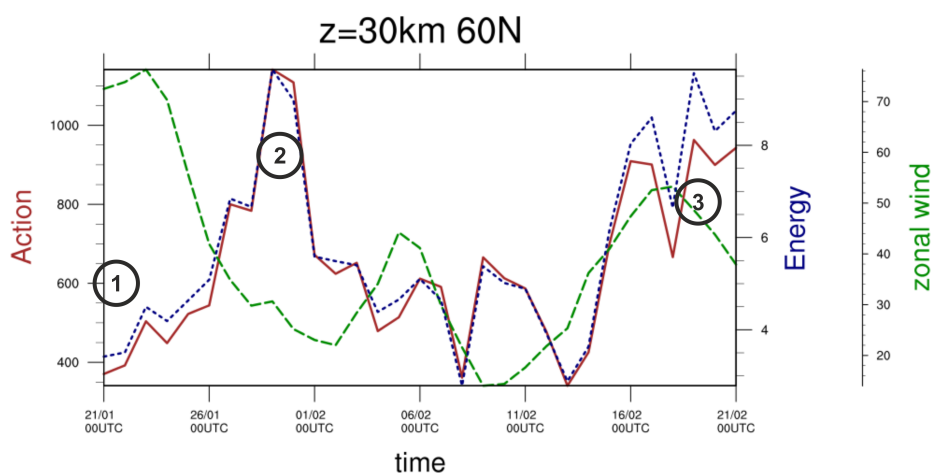


**Figure 3.** Time series from 21 January 2016 to 21 February 2016 of wave action [ $\text{kg m}^{-1}\text{s}^{-1}$ ] (red), kinematic wave energy [ $\text{m}^2\text{s}^{-2}$ ] (blue) and zonal wind [ $\text{ms}^{-1}$ ] (green) at 30 km altitude and 60°N. The circled numbers mark three time steps for the analysis.

propagating in a horizontally homogenous wind  $u(z)$ , one has to accept that the energy scales with the background wind  $u$ .

Hence, wave action is used primarily for the following analysis. The effect of density and wind on the profiles of wave energy is discussed for selected examples.

## 5 3 Results

### 3.1 The stratospheric conditions in winter 2016

A period of interesting wind features during winter 2016 is chosen to be 21 January to 21 February 2016. Figure 3 shows the zonal wind in green at an altitude of 30 km and 60° N. This time series is characterised by strong wind fluctuations. Notable features are the high wind speeds at the beginning of the period followed by the first mSSW. It takes place on 2 February 2016 with an increase of zonal wind speed afterwards and a second slightly stronger mSSW on 9 February 2016, again followed by a wind increase. Besides the zonal wind, GW characteristics are shown (kinematic wave energy and wave action). The small differences between kinematic wave energy and wave action are caused by the wind effect. Differences occur on dates where the zonal wind speed is high, pointing out the scaling of kinematic wave energy with the wind. A change in wave action is supposed to be caused by a variation in the intrinsic frequency hinting at a steepening of GWs.

Application of UWaDi reveals the following mean GW properties for the time period from 21 January to 21 February 2016: The horizontal wavelength ranges between 361 km and 499 km with a mean value of 414 km and shows no height depen-



dence. This is well above the smallest sampled horizontal wavelength of about 222 km regarding the sample theorem. The vertical wavelength appears to depend strongly on the wind. Respectively, the vertical wavelength has the lower limit of 3.31 km, which is larger than the sampling limit of 2 km. The mean intrinsic period is found to be 9.7 h. This is a typical value for near-inertial GWs, which have a frequency close to the Coriolis frequency  $f$ . The mean intrinsic phase speed is  $13 \text{ m s}^{-1}$ . For the GW energy we find a mean value of  $23 \text{ m}^2 \text{ s}^{-2}$  in the zonal mean, while it can be locally much larger. The highest value of  $690 \text{ m}^2 \text{ s}^{-2}$  is found on 30 January 2016 at ( $60^\circ \text{ N}$ ,  $20^\circ \text{ E}$ ). It appears in a region with high GW activity over Northern Europe (Fig. 4b).

How can the diagnosed GW properties during this minor warming be related to long-term characteristics? The horizontal wavelength appears to be slightly larger than the multi-year winter range of 238 km to 398 km as derived from radiosonde data at Lindenberg ( $52^\circ \text{ N}$ ,  $14^\circ \text{ E}$ ) for the lower stratosphere (12 km to 19 km) (Schöllhammer, 2002). The vertical wavelength, instead is definitively larger than the multi-year winter mean of Lindenberg which is 2.2 km to 2.5 km. The GW energy is far above the Lindenberg values which are between  $3.9 \text{ m}^2 \text{ s}^{-2}$  and  $7.2 \text{ m}^2 \text{ s}^{-2}$ . It is also far more than the maximal value of  $71.8 \text{ m}^2 \text{ s}^{-2}$  obtained from 10 radiosonde campaigns ran at Kühlungsborn ( $54^\circ \text{ N}$ ,  $12^\circ \text{ E}$ ) (Zülicke and Peters, 2008). Do we deal with a special atmospheric situation which deviates largely from the long-term characteristics? Can we explain the diagnosed GW properties in terms of generation and propagation?

Naively, one would expect high GW activity for strong zonal mean zonal wind and vice versa. Under this aspect, three periods show interesting features (marked in Fig 3 as ①, ②, ③). For these three periods the stratospheric situation is reviewed (Fig. 4). Figure 4a shows the horizontal divergence and the wind velocity together with the geopotential for the prewarming case ① on 22 January 2016 at 30 km altitude. The geopotential shows a strong polar vortex centred over the north pole with a nearly uniform distributed wind except wind deceleration areas above the USA. The horizontal divergence as an indicator for GW activity shows features alongside the edge of the polar vortex. These patterns are described as characteristic for the prewarming phase ① and are found in simulations, too (Limpasuvan et al., 2011). They are supposed to be westward propagating GWs excited by topography about ten days before the SSW. Observations as well as simulations declare that their wave characteristics show typical orographic features. In the upper stratosphere their vertical wavelengths are comparatively long because the short waves are filtered out by strong winds around the polar edge. In the zonal mean around the  $60^\circ$ -longitude and in 30 km altitude GW activity is low, while strong winds are present (Fig. 3). The polar-edge GW maximum has to be analysed locally to find comparable results to measurements in that area (Yamashita et al., 2010).

Figure 4b belongs to the period around the midwarming ②, 30 January 2016. The geopotential shows a displacement of the polar vortex coming along with a non-uniform distribution of the wind around the vortex. Wind speed is enhanced above the pole and decelerated over eastern Europe. In this area increased GW activity can be observed in the horizontal divergence field over Northern Europe. Indeed, the deceleration area of a jet stream is a possible source for GWs (O'sullivan and Dunkerton, 1995; Zülicke and Peters, 2008; Plougonven and Zhang, 2014). This fits to the peak in wave characteristics seen in the time series (Fig. 3), although the zonal-mean zonal wind is relatively weak.

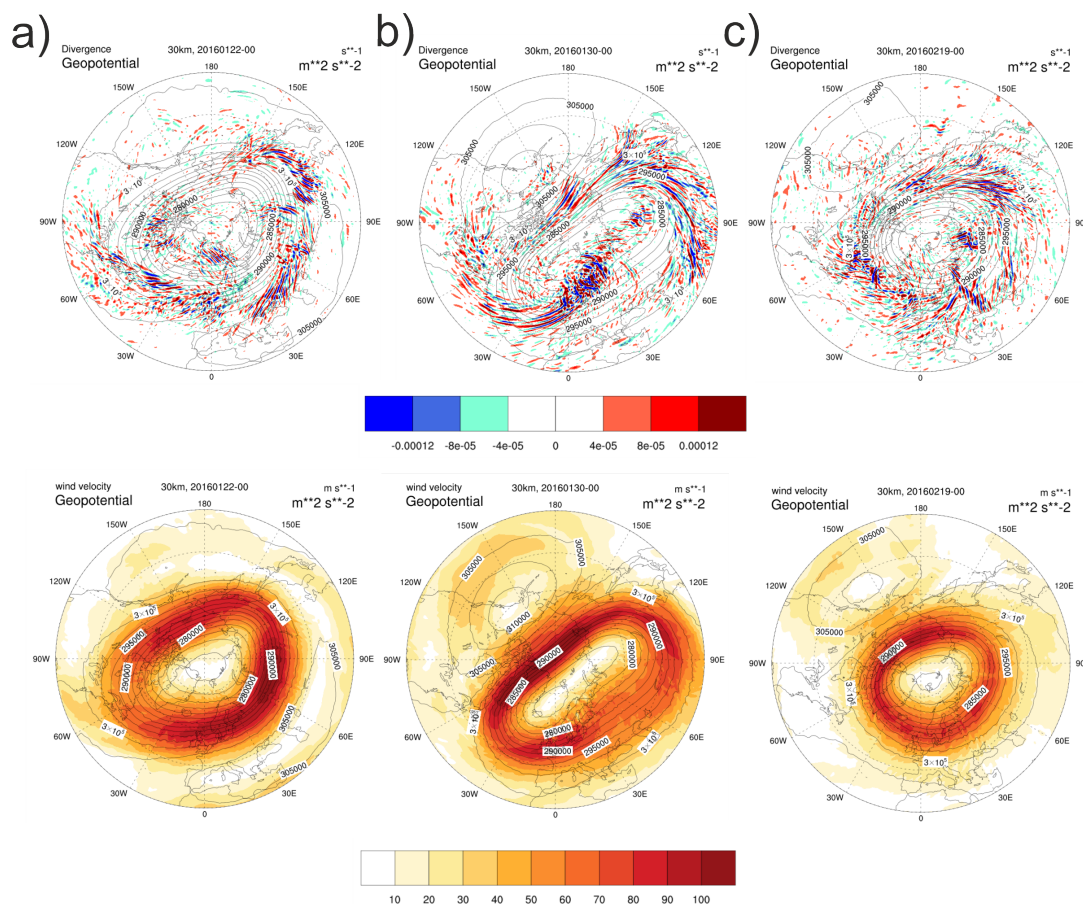


**Figure 4.** Horizontal divergence [ $s^{-1}$ ] (upper row) and wind velocity [ $ms^{-1}$ ] (lower row) coloured with contours of geopotential [ $m^2s^{-2}$ ] for three time steps (columns) and 10 hPa altitude. a) 22 January 2016 ①, b) 30 January 2016 ② and c) 19 February 2016 ③.

Figure 4c shows a snapshot from the postwarming phase ③, 19 February 2016. This date is characterised by a polar vortex with uniform distributed wind nearly centred above the pole. The horizontal divergence field shows much more fluctuations than on 22 January 2016 and therefore the time series (Fig. 3) shows higher values in wave characteristics in the postwarming phase. With regard to the zonal mean zonal wind, such an enhanced GW activity is expected.

### 5 3.2 Case ① (22 January 2016)

UWaDi provides wave properties locally, hence the difference between the three selected cases can be analysed for differences in GW generation and propagation for local and zonal mean quantities. The main focus is on vertical wave propagation since the horizontal wave number can be assumed to be constant with height, which is proven in Fig. 5. It shows horizontal wave numbers corresponding to wavelengths between 359 km and 433 km. The vertical wave number is changing between zero and

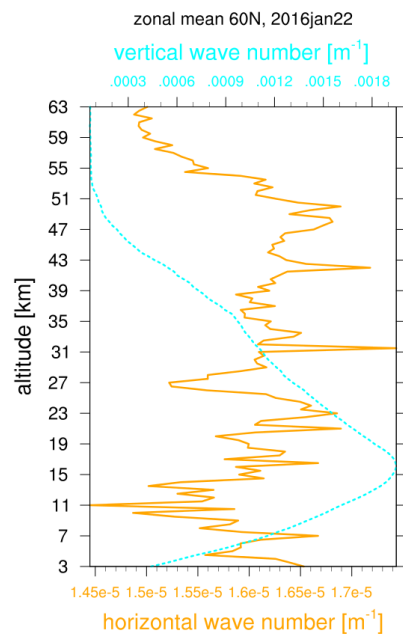


**Figure 5.** Comparison between horizontal (orange) and vertical wave number (cyan) [ $\text{m}^{-1}$ ] in zonal mean at  $60^\circ\text{N}$  against altitude for ①, 22 January 2016

a corresponding wavelength of 3.2 km. Hence, the horizontal wave number variation is small and the single-column model is sufficient to explain vertical GW propagation in different wind regimes.

A longitude-height section of the zonal wind at  $60^\circ\text{N}$  shows the wind distribution for the 22 January 2016 in the prewarming phase ① (Fig. 6a). The zonal wind has a strong westerly orientation in the stratosphere with a maximum above 10 hPa. The troposphere rather shows an alternating pattern caused by PWs meandering around the  $60^\circ\text{N}$  latitude leading to wind reversals in the troposphere. The longitude-height section of the wave action (Fig. 6b) shows enhanced GW action in the troposphere in westerlies as well as easterlies but GWs are clearly suppressed above an altitude of 19 km. In the zonal mean height-section (Fig. 6c) the zonal mean wind reversal is not strong and the wind is decreased to zero wind speed only at the surface. Wave action is strong in the troposphere, begins decreasing at 11 km altitude, right after the tropopause where a little wind minimum is visible. An even stronger decrease occurs above 19 km height which leads to a very weak GW signal in the middle stratosphere at 30 km altitude (c.f. Fig. 3). This decrease of the zonal mean action cannot be reasonably related to the increase in zonal mean wind. The zonal mean energy (Fig. 6c) peaks with the wind maximum at 36 km altitude. This finding contributes to our understanding to the density decrease with height which is not considered for the kinematic wave energy. Additionally, the wind effect is causing the kinematic wave energy scaling with the background wind. The downshift from the peak of kinematic wave energy to the peak of wave action can be explained by the relation between both quantities. Assuming

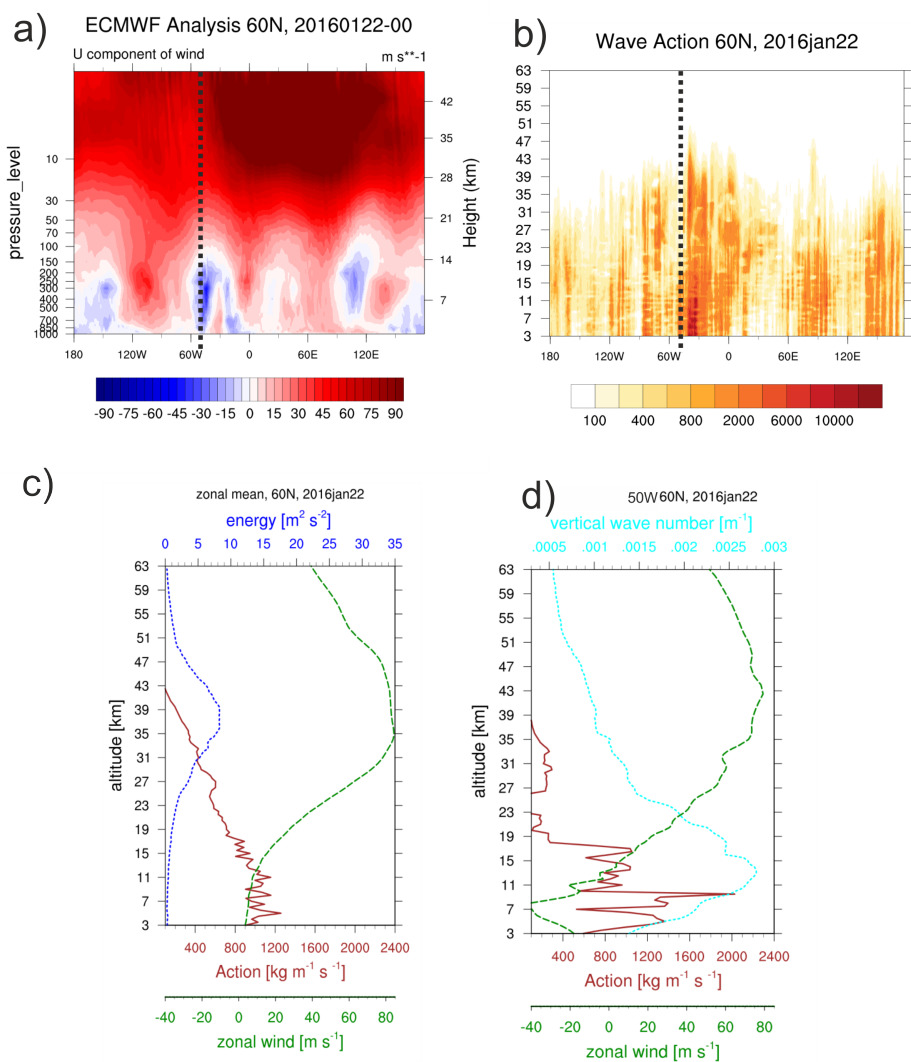


**Figure 6.** Wave analysis for ①, 22 January 2016 at 60°N. a) Zonal wind [ $\text{ms}^{-1}$ ] in a longitude-height cross-section. b) Wave action [ $\text{kg m}^{-1} \text{s}^{-1}$ ] in logarithmic scaling in a longitude-height cross-section. c) Zonal mean of wave action [ $\text{kg m}^{-1} \text{s}^{-1}$ ] (red), wave kinematic energy [ $\text{m}^2 \text{s}^{-2}$ ] (blue) and zonal wind (green) against altitude. d) Local wave properties at 50°W. Vertical wave number [ $\text{m}^{-1}$ ] (cyan), wave action (red) and zonal wind (green).



gaussian shape distributions and looking for the maximum explains the downshift of peak from about 35 km in kinematic wave energy to about 20 km in wave action.

The local analysis provides an insight into the wind constellation with a wind reversal. A section through 50° W is shown in Fig. 6d. Instead of the kinematic wave energy the vertical wave number is plotted. In the troposphere high easterlies occur. The wind reversal takes place at 15 km height and afterwards very strong westerlies build up. These winds first filter out the westward propagating GWs in the troposphere and by changing to strong eastward winds, the eastwards propagating GWs are suppressed. Hence, ending up with very weak GW activity in the stratosphere. A first decrease in wave action is visible where  $u = -15\text{m s}^{-1}$  is passed, the second decrease occurs where  $u \approx 15\text{m s}^{-1}$  is reached at 19 km. The vertical wave number peak is an indicator for wave absorption according to the dispersion relation and definition of the Doppler frequency:  $k_z = \frac{N}{(c-u)}$ . Knowing the mean horizontal phase speed of  $c = \pm 13\text{m s}^{-1}$ , which can be calculated with the local wave properties of UWaDi, winds of this order yield to a wave number increase by reducing the denominator to zero.

Summing up, local critical-level absorption takes place in a situation with strong zonal mean zonal wind accompanied with strong PWs. In this case one can envision the valve is closed locally which leads to a decreasing zonal mean GW activity. Comparing this result to the synoptical situation shows little fluctuations in horizontal divergence at 60° N and 50° W. The polar edge with enhanced GW activity is found slightly more to the North.

### 3.3 Case ② (30 January 2016)

An interesting situation with GW propagation up to the middle stratosphere is the midwarming phase ②. The 30 January 2016 shows a high peak in GW quantities although zonal wind speed is very low (Fig. 3). The longitude-height section of the zonal wind shows the mSSW features (Fig. 7a). The polar vortex displacement is visible by the easterlies in the upper stratosphere (compare Fig. 4b). The wave action in the longitude-height section shows a distinct area of propagating GWs during the SSW and areas where GWs are forbidden (Fig. 7b). The propagating area corresponds to the comparable low westerlies and forbidden zones are found where winds are very low and the wind reversal follows in higher altitudes. In zonal mean the zonal wind shows no reversal (Fig. 7c). By assessing the single-column model of vertical wave propagation, the signals can be explained and an open valve for GW transmission is found. The midwarming phase shows higher wave action in the troposphere than during strong wind conditions ①, decreasing until the height of  $u_c$  and increasing again with further increase of wind speed. Overall, the wind speed is low and lower wave action is expected. A second wind minimum is found at 43 km but GW signals are not reliable any more in that altitude because ECMWF damping is already active.

The local analysis gives a better insight and explains the high wave action in the zonal mean. A longitudinal profile at 20° E is a case of an open valve with eastward wind over the whole height range (Fig. 7d). Clearly visible is a wave-like structure of an estimated vertical wave length of 4 km to 5 km overlaying the overall shape of the zonal wind compared to the zonal mean (Fig. 7b). This does indeed hint at strong GW activity. Instead of wind filtering and GW attenuation at the critical level, locally advantageous wind conditions allow for an effective upward propagation. Indeed, the wave guide with winds exceeding  $15\text{ms}^{-1}$  is 15° wide and shows a wave action peak of about  $22000\text{kg m}^{-1}\text{s}^{-1}$ , one magnitude higher than in zonal mean. The

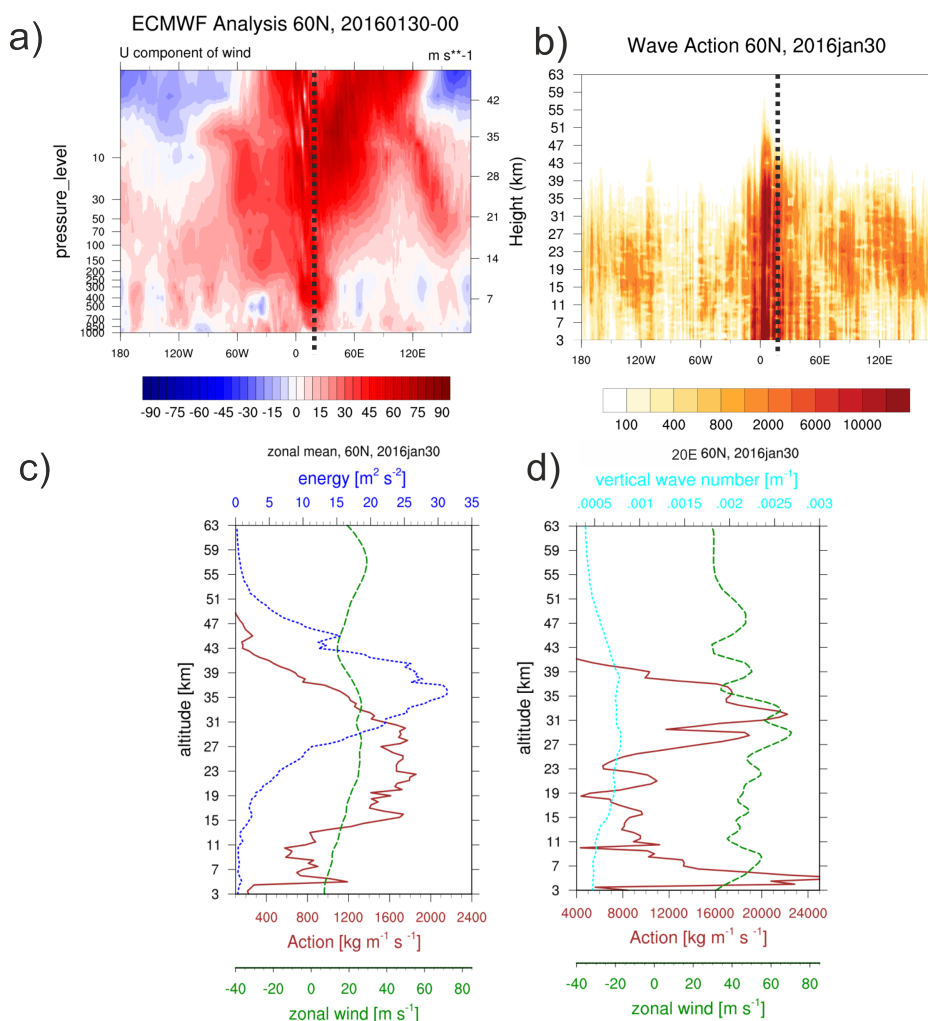


**Figure 7.** Wave analysis for ②, 30 January 2016 at 60°N. a) Zonal wind [ms<sup>-1</sup>] in a longitude-height cross-section. b) Wave action [kg m<sup>-1</sup>s<sup>-1</sup>] in logarithmic scaling in a longitude-height cross-section. c) Zonal mean of wave action [kg m<sup>-1</sup>s<sup>-1</sup>] (red), wave kinematic energy [m<sup>2</sup>s<sup>-2</sup>] (blue) and zonal wind (green) against altitude. d) Local wave properties at 50°W. Vertical wave number [m<sup>-1</sup>] (cyan), wave action (red) and zonal wind (green).

contribution of this wave guide to the zonal mean is 1800 kg m<sup>-1</sup>s<sup>-1</sup> which is round-about the zonal-mean value. Hence, this local valve explains the stratospheric GW activity seen in Fig. 3.

Wave activity has its maximum at about 30 km but it is also strong in the troposphere. Such GW valve layers were already found at the southern hemisphere during the "Deep Propagating Gravity Wave Experiment" (DEEPWAVE) field campaign (Fritts et al., 2016). They act as transmission channels for GWs with small-amplitudes (Kruse et al., 2016). Other studies show



the existence of the peak in GW enhancement right before the SSW but are restricted to zonal-mean measures (Yamashita et al., 2010; Jia et al., 2015). Obviously, the UWaDi algorithm can help to identify local valves explaining the GW enhancement before SSWs, when PWs are active.

Furthermore, it is shown that maximum GW amplitudes do not always correspond to areas of strongest winds by comparing the prewarming ① and midwarming phase ② with each other. Even though phase ② is defined by lower wind velocities than phase ①, GWs can propagate higher during phase ② due to an open valve. However, observations show that strongest wind areas do not always come together with high GW activity (Jia et al., 2015; Ern et al., 2016). Also for the midwarming phase ② the ECMWF sponge layer beginning at 30 km clearly attenuates the wave activity (Fig. 7d).

### 3.4 Case ③ (19 February 2016)

Previous studies by measurements as well as simulations show that GW strength does not develop to comparable high values in the postwarming phase than in the prewarming phase (Yamashita et al., 2010; Ern et al., 2016). Our findings do not support this for the case study on 19 February 2016 ③ (Fig. 8). This postwarming phase is characterised by high wave activity up to the middle stratosphere (Fig. 3). The wind speeds in the stratosphere are slightly weaker than in the prewarming phase ① ( $\approx 15\text{m s}^{-1}$ , see Fig. 6a and 8). However, the troposphere is more uniformly populated by westerlies meaning that the tropospheric jet meanders less around the  $60^\circ$  N-latitude. The wave action at the  $60^\circ$  N-longitude shows GW activity broadly distributed in the middle stratosphere compared to the cases before (Fig. 8b). Especially high propagating GWs are maintained in areas of westerlies comparable to the open valve already described in phase ②.

In the zonal mean GW analysis (Fig. 8c) the zonal wind speed shows values above  $u_c$  for the whole height. Therefore GW propagation is not suppressed by wind filtering applying the single-column theory. Wave action peaks at 20 km altitude and decreases until a second local maximum at 35 km altitude. Afterwards the damping of wave on ECMWF suppresses any further propagation.

One more striking feature might be a normal case with decreasing wind in the troposphere, a clearly distributed tropospheric jet and afterwards again decreasing wind velocities in the stratosphere. This happens in the section around the  $28^\circ$  W-latitude, where a local profile is taken (Fig. 8d). The local analysis covers a height range of consistently eastward wind and additionally shows the vertical wave number. This section is characterised by a proper tropospheric and stratospheric jet. Nevertheless, the wind does not reach  $u_c$  thus GW propagation is not restrained. Wave action peaks less in the troposphere than in the stratosphere. Furthermore, a minimum can be seen in the height of the valve at about 18 km, additionally with the peak in the vertical wave number this accounts for an absorption of GWs. Wave action increases again showing that GWs still propagate vertically. It is damped by ECMWF from 30 km on. The vertical wave number peaks again at 39 km coming together with the small peak in wave action showing another wave absorption event in that altitude but ECMWF damping obsoletes any deeper look on it.

Interestingly, the GW action in the midwarming case ② and the postwarming case ③ is about ten times higher although the wind profiles are of similar range (compare Fig. 7d with 8d). We may speculate on different wave generation processes in these cases. Whether the source mechanism during the postwarming phase ③ is not further studied here, we have already claimed

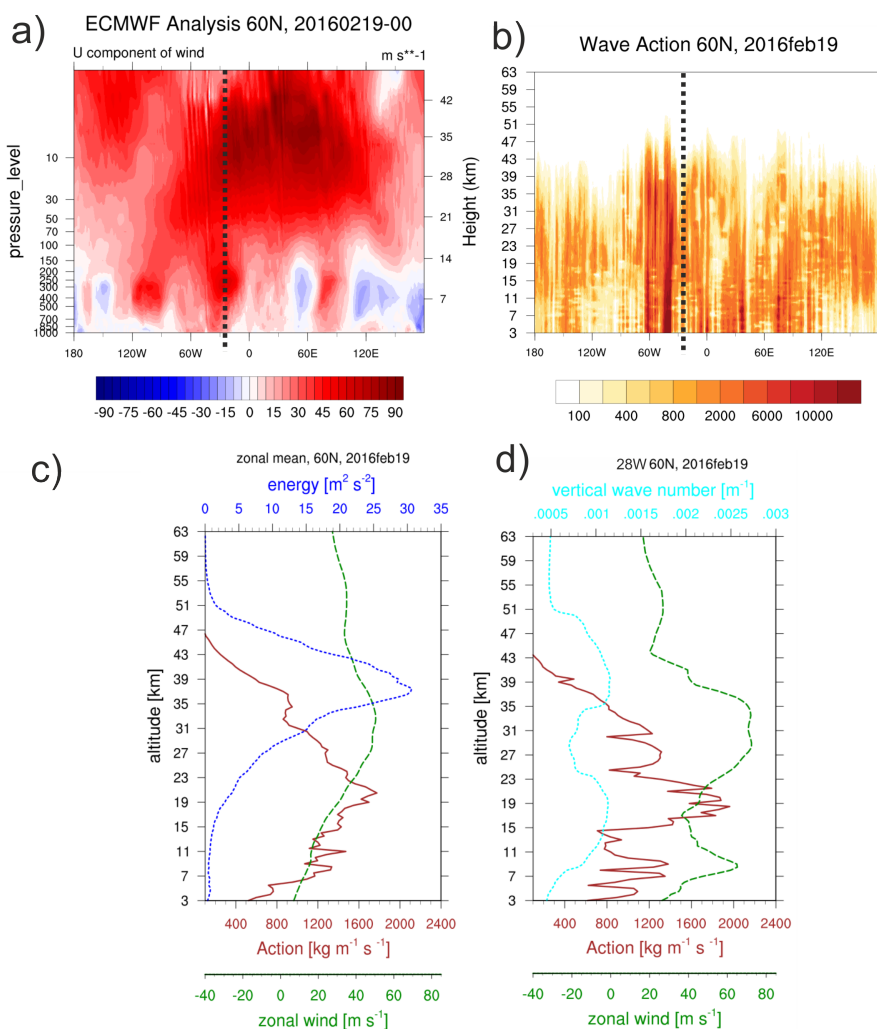


**Figure 8.** Wave analysis for ③, 19 February 2016 at 60°N. a) Zonal wind [ $\text{ms}^{-1}$ ] in a longitude-height cross-section. b) Wave action [ $\text{kg m}^{-1} \text{s}^{-1}$ ] in logarithmic scaling in a longitude-height cross-section. c) Zonal mean of wave action [ $\text{kg m}^{-1} \text{s}^{-1}$ ] (red), wave kinematic energy [ $\text{m}^2 \text{s}^{-2}$ ] (blue) and zonal wind (green) against altitude. d) Local wave properties at 50°W. Vertical wave number [ $\text{m}^{-1}$ ] (cyan), wave action (red) and zonal wind (green).

GW source for the midwarming case ②: The intense GW field near the jet-exit region over Northern Europe is a constellation preferable to spontaneous radiation of GWs.

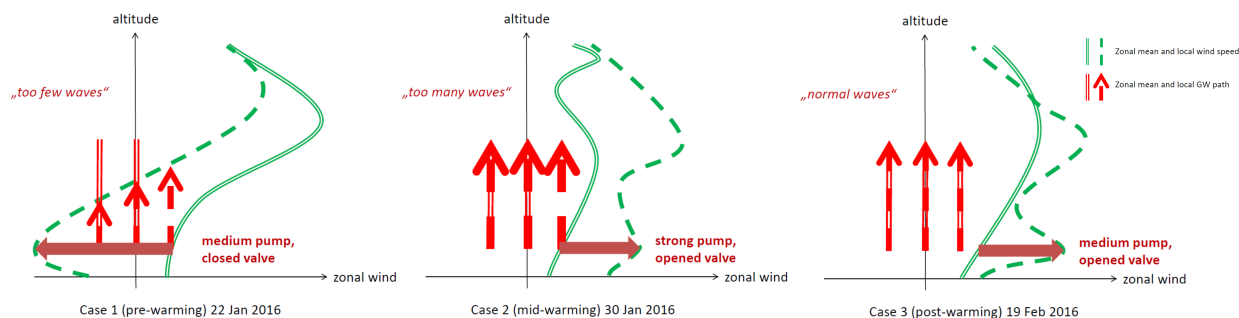


**Figure 9.** Schemes of GW paths (red) and zonal wind (green) for zonal mean (bold line) and locally (dashed) for phase ①, ② and ③.

#### 4 Conclusions

A diagnostic tool for studies of wave packets is developed and applied. The Unified Wave Diagnostics (UWaDi) uses the Hilbert Transform to obtain a complex signal from a real-valued function and estimates the amplitude and wave number locally. Although applicable to any wave-like signal, we specified it to detect gravity waves. The procedure leads to reliable results for synthetic test cases and operational analysis data. The lack of sign of the estimated wave numbers by UWaDi can be overcome by implementing a frequency-wave number analysis. This will help improving the understanding of GW propagation, whereas directions of propagations can be put into relation to the background wind vector.

The analysis of ECMWF-IFS data shows resolved GWs in the troposphere and stratosphere. However, above an altitude of 1 hPa no systematic waves could be found and even above 10 hPa the first sponge layer starts and the results have to be interpreted with care. We use these data to demonstrate the different patterns of wave action and wave energy. As expected, the kinematic wave energy strongly depends on density and wind profiles and might establish a maximum while the wave action does not peak at this location. We have shown this for zonal-mean profiles and decided to use the wave action for the wave analysis.

We study a minor sudden stratospheric warming (mSSW) event including strong zonal wind variations in space and time. The usual expectation is that high zonal-mean zonal wind causes high wave activity. We analysed three different situations and identified valves and pumps of GWs. First, a low-wind region near the tropopause causes low GW action while the stratospheric wind is high during the prewarming phase ①. This is an example for a closed valve (Fig. 9-①). Second, better propagation conditions are found during the midwarming phase ②, where an open local valve with high westerlies in a situation when the stratospheric wind is low, makes it possible for GWs to propagate into the stratosphere and cause GW action substantially higher than in any other period. Additionally, the GW generation in the troposphere was found to be enhanced. Hence, the GW pump was running high (Fig. 9-②). Third, GW propagation was also analysed for the postwarming phase ③ where the mid-stratospheric wind reinforced again and GW action is smaller than during the midwarming phase ②. Here, both the zonal mean and the local wind fields permitted GW propagation and the stratospheric wave activity was passing the valve as expected while the GW pump was running normal (Fig. 9-③). These three cases demonstrate that for the evaluation of GW activity at a



certain altitude its whole propagation history through the layers below has to be taken into account. In particular during SSWs the structure of PWs may modify the local GW generation (pump) and transmission (valve) considerably.

In some cases (②,③) we detected secondary peaks in the wave action profiles. This might be associated to non-tropospheric wave generation. Possible candidates are the tropospheric and the stratospheric jet. These two cases are also described by similar wind conditions but different wave distributions which also might be due to different wave generation processes. It was just the midwarming case ② at 30 January 2016 at 60° N 20° W for which we found an extraordinarily high GW activity at 10 hPa. This occasion was also covered by the ROMIC/GW-LCYCLE campaigns and might deserve special attention.

Besides the particular application of UWaDi to GWs and SSWs, the tool was already successfully tested to identify wave packet properties in rotating annulus experiments (Hien et al.). Recapitulatory, the study of SSW is a good test case for GWs due to the high spatio-temporal variability due to PW activity. This changes not only the propagation conditions locally in a drastic way, but also gives rise to changing wave generation.

*Code and data availability.* The data from ECMWF is accessible through the archive of [www.ecmwf.int](http://www.ecmwf.int) provided by the Deutscher Wetterdienst. The code named UWaDi is available through the authors. It is coded in open-source software and an user's manual is provided. The authors request to cite this paper in case of applying the UWaDi algorithm.

15 *Competing interests.* The authors declare that no competing interests are present.

*Acknowledgements.* We acknowledge the funding of the research unit Multiscale Dynamics of Gravity Waves / project Spontaneous Imbalance by the Deutsche Forschungsgemeinschaft (DFG) through grant ZU 120/2-1. Furthermore the authors want to thank the ECMWF for data supply and the WRF user support at NCAR for the assistance provided with the data processing with WPS. Useful comments on this manuscript were given by Vivien Matthias and Steffen Hien.



## References

- Albers, J. R. and Birner, T.: Vortex preconditioning due to planetary and gravity waves prior to sudden stratospheric warmings, *Journal of the Atmospheric Sciences*, 71, 4028–4054, 2014.
- Andrews, D. G., Holton, J. R., and Leovy, C. B.: *Middle atmosphere dynamics*, 40, Academic press, 1987.
- 5 Bretherton, F. P.: The propagation of groups of internal gravity waves in a shear flow, *Quarterly Journal of the Royal Meteorological Society*, 92, 466–480, 1966.
- De Wit, R., Hibbins, R., and Espy, P.: The seasonal cycle of gravity wave momentum flux and forcing in the high latitude northern hemisphere mesopause region, *Journal of Atmospheric and Solar-Terrestrial Physics*, 127, 21–29, 2015.
- Dunkerton, T. J. and Butchart, N.: Propagation and selective transmission of internal gravity waves in a sudden warming, *Journal of the*
- 10 *atmospheric sciences*, 41, 1443–1460, 1984.
- ECMWF: Part III: Dynamics and Numerical Procedures, IFS Documentation, ECMWF, 2016.
- Ern, M., Thai, Q., John, C., Martin, G., James, M., and Michael, J.: Satellite observations of middle atmosphere gravity wave absolute momentum flux and of its vertical gradient during recent stratospheric warmings, *Atmos. Chem. Phys.*, 1680, 7324, 2016.
- Fritts, D. C. and Alexander, M. J.: Gravity wave dynamics and effects in the middle atmosphere, *Reviews of Geophysics*, 41, 2003.
- 15 Fritts, D. C., Smith, R. B., Taylor, M. J., Doyle, J. D., Eckermann, S. D., Dörnbrack, A., Rapp, M., Williams, B. P., Pautet, P.-D., Bossert, K., et al.: The Deep Propagating Gravity Wave Experiment (DEEPWAVE): An airborne and ground-based exploration of gravity wave propagation and effects from their sources throughout the lower and middle atmosphere, *Bulletin of the American Meteorological Society*, 97, 425–453, 2016.
- Glatt, I. and Wirth, V.: Identifying Rossby wave trains and quantifying their properties, *Quarterly Journal of the Royal Meteorological*
- 20 *Society*, 140, 384–396, 2014.
- Hien, S., Rolland, J., Borchert, S., Schoon, L., Zülicke, C., and Achatz, U.: Spontaneous gravity wave emission in the differentially heated rotating annulus experiment, *Journal of Fluid Mechanics*, conditionally accepted.
- Hitchcock, P. and Shepherd, T. G.: Zonal-mean dynamics of extended recoveries from stratospheric sudden warmings, *Journal of the Atmospheric Sciences*, 70, 688–707, 2013.
- 25 Jewtoukoff, V., Hertzog, A., Plougonven, R., de la Cámara, A., and Lott, F.: Comparison of gravity waves in the Southern Hemisphere derived from balloon observations and the ECMWF analyses, *Journal of the Atmospheric Sciences*, 2015.
- Jia, Y., Zhang, S., Yi, F., Huang, C., Huang, K., Gan, Q., and Gong, Y.: Observations of gravity wave activity during stratospheric sudden warmings in the Northern Hemisphere, *Sci China Tech Sci*, 2015.
- Kinoshita, T. and Sato, K.: A formulation of three-dimensional residual mean flow applicable both to inertia–gravity waves and to Rossby
- 30 waves, *Journal of the Atmospheric Sciences*, 70, 1577–1602, 2013a.
- Kinoshita, T. and Sato, K.: A formulation of unified three-dimensional wave activity flux of inertia–gravity waves and Rossby waves, *Journal of the Atmospheric Sciences*, 70, 1603–1615, 2013b.
- Kinoshita, T. and Sato, K.: A formulation of three-dimensional residual mean flow and wave activity flux applicable to equatorial waves, *Journal of the Atmospheric Sciences*, 71, 3427–3438, 2014.
- 35 Kruse, C. G., Smith, R. B., and Eckermann, S. D.: The Midlatitude Lower-Stratospheric Mountain Wave „Valve Layer”, *Journal of the Atmospheric Sciences*, 73, 5081–5100, 2016.



- Limpasuvan, V., Alexander, M. J., Orsolini, Y. J., Wu, D. L., Xue, M., Richter, J. H., and Yamashita, C.: Mesoscale simulations of gravity waves during the 2008–2009 major stratospheric sudden warming, *Journal of Geophysical Research: Atmospheres*, 116, 2011.
- Limpasuvan, V., Richter, J. H., Orsolini, Y. J., Stordal, F., and Kvissel, O.-K.: The roles of planetary and gravity waves during a major stratospheric sudden warming as characterized in WACCM, *Journal of Atmospheric and Solar-Terrestrial Physics*, 78, 84–98, 2012.
- 5 Liu, H.-L. and Roble, R.: A study of a self-generated stratospheric sudden warming and its mesospheric–lower thermospheric impacts using the coupled TIME-GCM/CCM3, *Journal of Geophysical Research: Atmospheres*, 107, 2002.
- Miller, A., Schmidt, H., and Bunzel, F.: Vertical coupling of the middle atmosphere during stratospheric warming events, *Journal of Atmospheric and Solar-Terrestrial Physics*, 97, 11–21, 2013.
- O’sullivan, D. and Dunkerton, T. J.: Generation of inertia-gravity waves in a simulated life cycle of baroclinic instability, *Journal of the*  
10 *Atmospheric Sciences*, 52, 3695–3716, 1995.
- Plougonven, R. and Zhang, F.: Internal gravity waves from atmospheric jets and fronts, *Reviews of Geophysics*, 52, 33–76, 2014.
- Plougonven, R., Teitelbaum, H., and Zeitlin, V.: Inertia gravity wave generation by the tropospheric midlatitude jet as given by the Fronts and Atlantic Storm-Track Experiment radio soundings, *Journal of Geophysical Research: Atmospheres*, 108, 2003.
- Plumb, R. A.: On the three-dimensional propagation of stationary waves, *Journal of the Atmospheric Sciences*, 42, 217–229, 1985.
- 15 Plumb, R. A.: Three-Dimensional Propagation of Transient Quasi-Geostrophic Eddies and Its Relationship with the Eddy Forcing of the Time-Mean Flow, *Journal of the atmospheric sciences*, 43, 1657–1678, 1986.
- Preusse, P., Ern, M., Bechtold, P., Eckermann, S., Kalisch, S., Trinh, Q., and Riese, M.: Characteristics of gravity waves resolved by ECMWF, *Atmospheric chemistry and physics*, 14, 10 483–10 508, 2014.
- Sato, K., Kinoshita, T., and Okamoto, K.: A new method to estimate three-dimensional residual-mean circulation in the middle atmosphere  
20 and its application to gravity wave–resolving general circulation model data, *Journal of the Atmospheric Sciences*, 70, 3756–3779, 2013.
- Schöllhammer, K.: *Klimatologie der Schwerewellenaktivität in den mittleren Breiten (PhD Thesis)*, Phd, 2002.
- Schönwiese, C.-D.: *Praktische Statistik für Meteorologen und Geowissenschaftler*, Schweizerbart’sche Verlagsbuchhandlung, 2013.
- Shutts, G. and Vosper, S.: Stratospheric gravity waves revealed in NWP model forecasts, *Quarterly Journal of the Royal Meteorological Society*, 137, 303–317, 2011.
- 25 Skamarock, W. C., Klemp, J. B., Dudhia, J., Gill, D. O., Barker, D. M., Duda, M. G., Huang, X.-Y., Wang, W., and Powers, J. G.: A Description of the Advanced Research WRF Version 3, 2008.
- Thuraiajah, B., Bailey, S. M., Cullens, C. Y., Hervig, M. E., and Russell, J. M.: Gravity wave activity during recent stratospheric sudden warming events from SOFIE temperature measurements, *Journal of Geophysical Research: Atmospheres*, 119, 8091–8103, 2014.
- Uccellini, L. and Koch, S.: The synoptic setting and possible source mechanisms for mesoscale gravity wave events, *Mon. Weather Rev*, 115,  
30 721–729, 1987.
- Vincent, R. A. and Fritts, D. C.: A climatology of gravity wave motions in the mesopause region at Adelaide, Australia, *Journal of the atmospheric sciences*, 44, 748–760, 1987.
- Von Storch, H. and Zwiers, F. W.: *Statistical analysis in climate research*, Cambridge university press, 2001.
- Wu, D. L. and Eckermann, S. D.: Global gravity wave variances from Aura MLS: Characteristics and interpretation, *Journal of the Atmospheric Sciences*, 65, 3695–3718, 2008.
- 35 Yamashita, C., Liu, H.-L., and Chu, X.: Gravity wave variations during the 2009 stratospheric sudden warming as revealed by ECMWF-T799 and observations, *Geophysical Research Letters*, 37, 2010.



- Yamashita, C., England, S. L., Immel, T. J., and Chang, L. C.: Gravity wave variations during elevated stratopause events using SABER observations, *Journal of Geophysical Research: Atmospheres*, 118, 5287–5303, 2013.
- Zimin, A. V., Szunyogh, I., Patil, D., Hunt, B. R., and Ott, E.: Extracting envelopes of Rossby wave packets, *Monthly weather review*, 131, 1011–1017, 2003.
- 5 Zimin, A. V., Szunyogh, I., Hunt, B. R., and Ott, E.: Extracting envelopes of nonzonally propagating Rossby wave packets, *Monthly weather review*, 134, 1329–1333, 2006.
- Zülicke, C. and Peters, D.: Simulation of inertia-gravity waves in a poleward-breaking Rossby wave, *Journal of the atmospheric sciences*, 63, 3253–3276, 2006.
- Zülicke, C. and Peters, D.: Parameterization of strong stratospheric inertia–gravity waves forced by poleward-breaking Rossby waves,  
10 *Monthly Weather Review*, 136, 98–119, 2008.